
This item was submitted to [Loughborough's Research Repository](#) by the author.
Items in Figshare are protected by copyright, with all rights reserved, unless otherwise indicated.

Effects of temperature and microstructure on low cycle fatigue behaviour of a PM Ni-based superalloy: EBSD assessment and crystal plasticity simulation

PLEASE CITE THE PUBLISHED VERSION

<https://doi.org/10.1016/j.ijfatigue.2022.106818>

PUBLISHER

Elsevier

VERSION

AM (Accepted Manuscript)

PUBLISHER STATEMENT

This paper was accepted for publication in the journal International Journal of Fatigue and the definitive published version is available at <https://doi.org/10.1016/j.ijfatigue.2022.106818>.

LICENCE

CC BY-NC-ND 4.0

REPOSITORY RECORD

Zhang, WT, R Jiang, Y Zhao, LC Zhang, L Zhang, Ligu Zhao, and YD Song. 2022. "Effects of Temperature and Microstructure on Low Cycle Fatigue Behaviour of a PM Ni-based Superalloy: EBSD Assessment and Crystal Plasticity Simulation". Loughborough University. <https://hdl.handle.net/2134/19207422.v1>.

Effects of temperature and microstructure on low cycle fatigue behaviour of a PM Ni-based superalloy: EBSD assessment and crystal plasticity simulation

W. T. Zhang ^{a, b}, R. Jiang ^{a, b, *}, Y. Zhao ^{a, b}, L.C. Zhang ^{a, b}, L. Zhang ^{a, b}, L.G. Zhao ^{a, b, c},
Y. D. Song ^{a, b, d}

a. Key Laboratory of Aero-engine Thermal Environment and Structure, Ministry of Industry and Information Technology, College of Energy and Power Engineering, Nanjing University of Aeronautics and Astronautics, Nanjing, 210016, PR China

b. Jiangsu Province Key Laboratory of Aerospace Power System, College of Energy and Power Engineering, Nanjing University of Aeronautics and Astronautics, Nanjing, 210016, PR China

c. Wolfson School of Mechanical, Electrical and Manufacturing Engineering, Loughborough University, LE11 3TU, United Kingdom

d. State Key Laboratory of Mechanics and Control Mechanical Structures, Nanjing University of Aeronautics and Astronautics, Nanjing, 210016, PR China

*Corresponding author. Email: rjiang@nuaa.edu.cn

Abstract

The macro and mesoscale deformation and damage of the PM nickel-based superalloy FGH4098 under low cycle fatigue loading at elevated temperatures were investigated using both SEM/EBSD characterization and crystal plasticity finite element (CPFE) simulations. The results indicate that higher temperature leads to more severe macroscale damage i.e. larger areas of hysteresis loops and shorter fatigue life with transgranular failure mode at both 650°C and 750°C. The misorientation parameters derived from EBSD characterization show similar deformation at both temperatures, but more intense localized deformation in the crack initiation region at 750°C. Based on the accumulated shear-strain energy dissipation density and Fatemi-Socie fatigue indicator parameter, the distribution and evolution of fatigue damage are shown to be strongly affected by local stress-strain state and temperatures, and more severe and homogeneous damage is found at 750°C. The CPFE simulation results also show higher damage propensity, as indicated by the fatigue indicator parameters used here, in the vicinity of annealing twin boundaries with high difference in elastic modulus.

Keywords: Low cycle fatigue; EBSD characterization; Crystal plasticity; Fatigue indicator parameter; PM Ni-based superalloy

Abbreviations

CPFE	crystal plasticity finite element
PM	powder metallurgy
LCF	low cycle fatigue
GROD	grain reference orientation deviation
KAM	kernel average misorientation
GND	geometrically necessary dislocation
HR-EBSD	high resolution electron backscattered diffraction
ASSED	accumulated shear-strain energy dissipation density
AOI	area of interest
IPF	inverse pole figure
CSL	coincidence site lattice
HAGB	high angle grain boundary
RSS	resolved shear stress
CRSS	critical resolved shear stress
UMAT	user-material subroutine
FIP	fatigue indicator parameter
EDD	energy dissipation density
CIS	crack initiation site
CPR	crack propagation region
FFR	final fracture region

1. Introduction

Powder metallurgy (PM) Ni-based superalloys have been widely used for turbine disks in high-performance aero-engines owing to their more favourable combined properties, i.e. higher strength at elevated temperatures, stronger resistance to fatigue, creep, oxidation and corrosion, compared to conventional wrought and cast Ni-based superalloys [1, 2]. Under

service conditions, aero-engine turbine disks are exposed to harsh environments and subjected to complex loading conditions, including cyclic mechanical loads, thermal stress and vibration stress. The resulting low cycle fatigue (LCF) failure is one of the most critical issues that restrict the structural integrity of aero-engines.

In order to avoid catastrophic failure of these key components, significant efforts have been made to study the deformation and LCF failure mechanisms of disk alloys, and to assess structural integrity of disk components by means of advanced experimental and simulation methods [3-5]. Generally speaking, the LCF behaviour of Ni-based superalloys especially in the regime of crack initiation and micro-crack propagation is strongly influenced by various grain-scale factors, such as elastic anisotropy [6], grain boundary features [7] and the interaction between intragranular slip and grain boundaries [8, 9]. Hence, investigation of the heterogeneity of deformation and damage is fundamental in understanding the role of these factors in LCF failure.

With the EBSD technique, crystallographic orientation data, especially the misorientation parameters, can be obtained and utilized in the analysis of fatigue [10], creep [11, 12] and creep-fatigue interactive deformation behaviour [13]. These misorientation related parameters mainly include grain reference orientation deviation (GROD), kernel average misorientation (KAM) and derived geometrically necessary dislocation (GND) density, which provide significant information of local deformation and dislocation movement. For instance, Rui et al. [12] established a linear correlation between creep strain and GROD, and developed a creep damage model considering external load level and experiment temperature for austenitic stainless steels. Wang et al. [13] conducted semi-quantitative creep-fatigue damage analysis of Ni-based superalloy GH4169 using KAM, GROD and GND, and suggested that these misorientation related parameters were consistent with the damage summation parameters derived from continuum damage mechanics under different dwell times and strain ratios. Furthermore, the correlation between these misorientation parameters and plastic strain was investigated by Harte [14] using high resolution digital image correlation. The results showed that the mean plastic strain is positively correlated with these misorientation parameters, but with a large scatter. In addition, recent advances in high resolution EBSD (HR-EBSD) allows quantification of elastic strain and lattice rotation based on image correlation of Kikuchi patterns and has been applied to comparison and validation of the simulation results [15-17].

Meanwhile, based on the characterization results using EBSD, finite element models considering realistic morphology, crystallographic orientation and microstructure features of the investigated alloys can be constructed [18, 19]. Based on the framework of crystal plasticity finite element (CPFE) method, several mesoscale slip related parameters have been proposed to investigate the deformation and damage under fatigue loadings, including effective plastic strain [5, 20, 21], accumulated shear-strain energy dissipation density (ASSED) [4, 22], the Fatemi-Socie parameter [23, 24] and the stored energy density [19, 25]. To date, CPFE modelling in regard to deformation heterogeneity in Ni-based superalloys are concentrated on the effects of grain size [26], inclusions [19, 21], annealing twin boundaries [6, 27] and external loads [28, 29]. However, there is limited research in evaluating the effect of temperature and microstructure on deformation and damage heterogeneity by taking advantage of CPFE simulation especially considering the realistic grain morphology and microstructure attributes.

Therefore, in this study, we aim to quantitatively investigate the effect of temperature and microstructure on the macro and mesoscale (at grain scale) deformation and damage behaviour of an advanced PM Ni-based superalloy FGH4098 under LCF. Firstly, the macroscale stress-strain response and corresponding SEM fractography are analysed under different temperatures, followed by assessment using the misorientation related parameters obtained from EBSD characterization of fractured specimens. Then the CPFE simulations based on realistic grain morphology based on 2D EBSD characterization are conducted with both ASSED and Fatemi-Socie fatigue damage parameters. Finally, the effect of annealing twin boundaries on heterogeneity of local deformation and damage is discussed.

2. Material and experiment methods

2.1 Materials

The material used in this study is the third-generation PM nickel-based superalloy FGH4098 manufactured by Central Iron and Steel Research Institute. Nominal composition (in wt. %) of FGH4098 alloy is 11-14Cr, 18-22Co, 3-4Mo, 2-3W, 3-4Al, 3-4Ti, 2-4Ta, 0.7-1.2Nb, 0.004O, 0.0006N, 0.00007H, Ni bal. The microstructure of this alloy consists of γ matrix phase and two populations of γ' precipitate phase (i.e. secondary γ' and tertiary γ' precipitate). The mean size of the secondary and tertiary γ' precipitates are 310 nm and 48nm, respectively [30]. The grain size distribution and grain boundary features are characterized by

EBSD analysis. Fig. 1 (a) and (c) present the Z-axis inverse pole figure (IPF) and pole figure of the FGH4098 alloy respectively, indicating there is no obvious texture in this material. Fig. 1 (b) shows the grain boundary and coincidence site lattice (CSL) boundary map, in which $\Sigma 3$ annealing twin boundaries are marked with red lines and account for 32.9% of the total boundary while high angle grain boundaries (HAGB) are plotted in black lines. The grain size obeys lognormal distribution approximatively and the mean value is 33.0 μm , as shown in Fig. 1 (d).

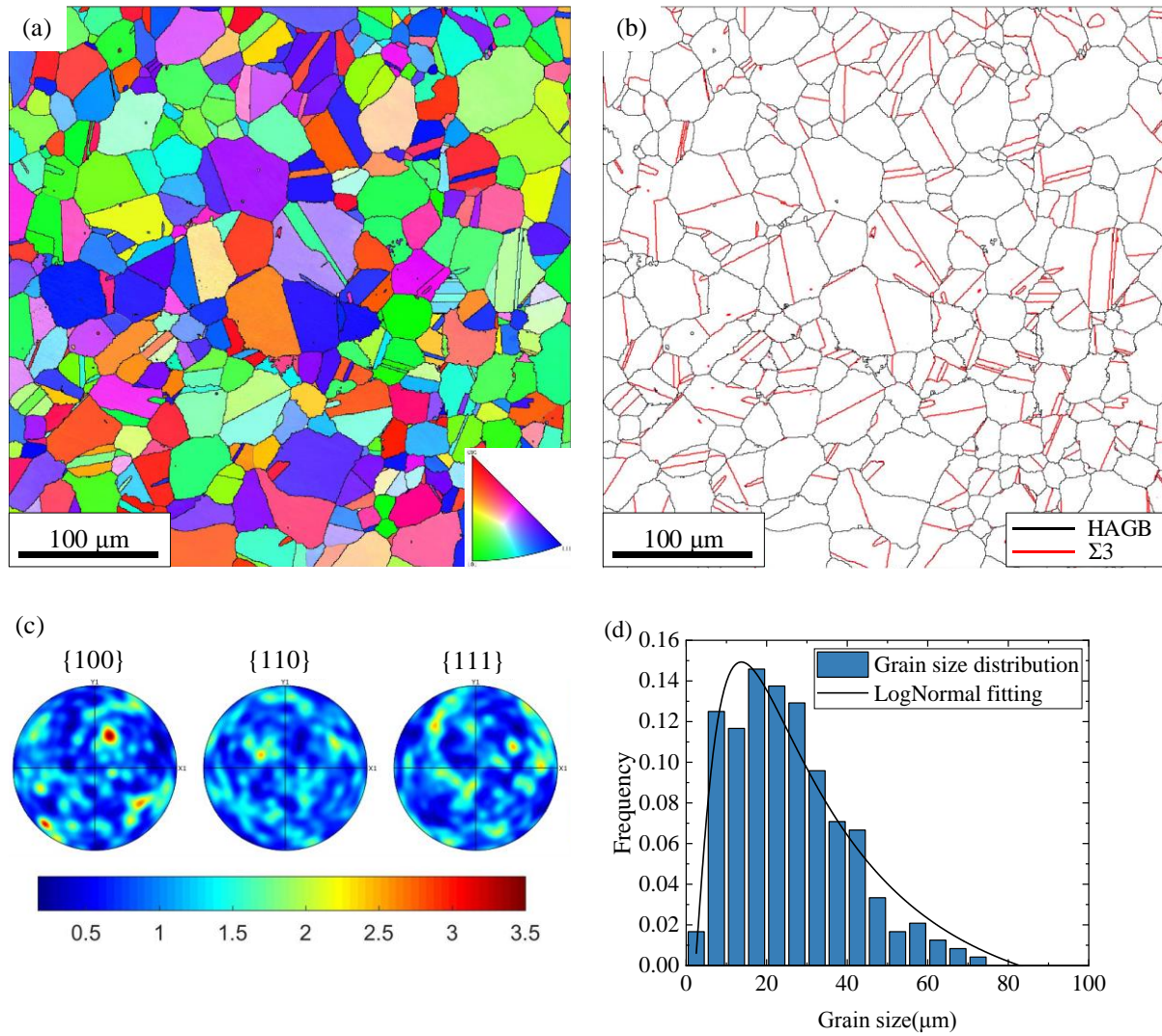


Fig. 1 (a) EBSD map of FGH4098 alloy with IPF colour. (b) Grain boundary and CSL boundary map. (c) $\{100\}$, $\{110\}$, $\{111\}$ pole figures. (d) Grain size distribution.

2.2 Low cycle fatigue tests

The dimensions of the LCF specimen employed here is shown in Fig. 2 (a). The LCF tests were conducted on a MTS Landmark370 testing machine under strain control according

to ASTM E606 standard. A MTS Model 632.51F-04 high temperature mechanical extensometer positioned at the gauge section measured strain value. The extensometer has a gage length of 12 mm and strain range from +20% to -10%. The strain range was set as 0.78% with a ratio of 0.05 and a 1-1-1-1 trapezoidal loading waveform was applied, as shown in Fig. 3. The strain rate is 0.78%/s during the loading and unloading stage. Four specimens were machined and two specimens each tested at 650°C and 750°C, respectively, in the air environment.

2.3 SEM and EBSD characterizations

After LCF tests, one of the fractured surfaces was used for SEM analysis, while the other one was cut along the longitudinal and transverse plane for EBSD measurements. It should be noted that, the longitudinal plane was cut parallel to the crack propagation direction from the crack initiation site with the assistance of predetermined marks, and transverse plane was cut about 5 mm away from the fracture surface avoiding severe deformation induced by final fracture. Two regions were selected as areas of interest (AOI), as illustrated in Fig. 2(b). AOI 1 in the centre of the transverse plane was selected to evaluate overall deformation level, while AOI 2 near the crack initiation site was aimed at studying local deformation in the crack initiation and propagation regime at different temperatures. The specimens were ground using grit sandpapers from #400 to #5000, and then electropolished for 10 s using a solution of 10 ml perchloric acid and 90 ml ethanol. EBSD measurements were performed on a Zeiss Gemini 300 field emission gun SEM equipped with an Oxford EBSD detector. In order to exclude the effects of EBSD acquisition parameters on misorientation related data of different specimens, a series of unified parameters were applied, i.e. 20.0 kV accelerating voltage, 60 μm aperture and 0.5 μm step size. Finally, the EBSD data was processed by Aztec Crystal software and open source toolbox MTEX [31], and the KAM and derived GND density maps were calculated with a 3 \times 3 kernel size.

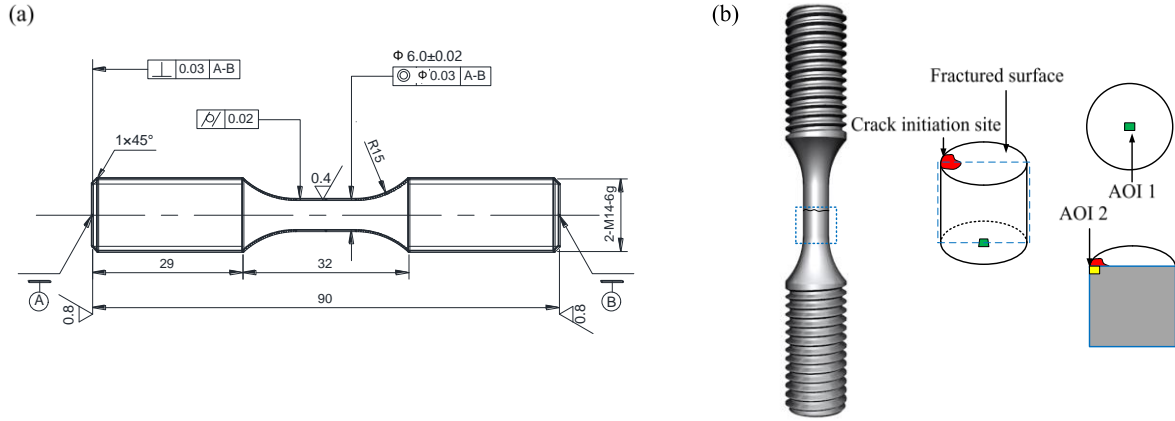


Fig. 2 (a) Dimensions of LCF specimens (in mm), and (b) Schematic diagram of fractured specimen with sectioning planes showing position for EBSD characterization.

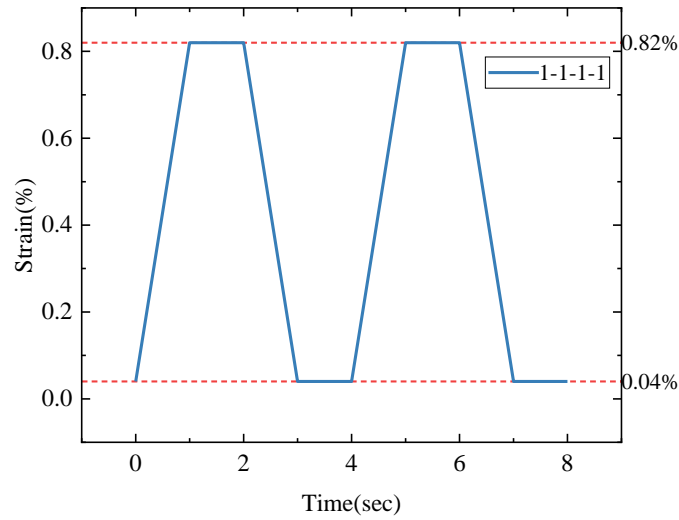


Fig. 3 Schematic diagram of the 1-1-1-1 trapezoidal loading waveform.

3. Crystal plasticity finite element modelling

3.1 Kinematics and kinetics

The rate dependent crystal plasticity constitutive model is developed based on the framework proposed by Huang [32]. It should be noted that inelastic deformation may be driven by dislocation slip, twinning, diffusion and grain boundary sliding [33-35]. For the limited loading level along with short loading period at elevated temperatures in the current study, crystallographic slip dominates the plastic deformation and damage. Plastic flow is assumed as a result of crystallographic slip, therefore.

The total deformation gradient \mathbf{F} can be decomposed by multiplicative decomposition:

$$\mathbf{F} = \mathbf{F}^e \mathbf{F}^p \quad (1)$$

where \mathbf{F}^e is the elastic portion accounting for deformation caused by stretching and rotation of the crystal lattice, and \mathbf{F}^p is the plastic portion accounting for crystallographic slip.

The velocity gradient \mathbf{L} is given by:

$$\mathbf{L} = \dot{\mathbf{F}} \cdot \mathbf{F}^{-1} = \dot{\mathbf{F}}^e \cdot \mathbf{F}^{e-1} + \mathbf{F}^e \cdot \dot{\mathbf{F}}^p \cdot \mathbf{F}^{p-1} \cdot \mathbf{F}^{e-1} \quad (2)$$

$$\mathbf{L} = \mathbf{D} + \mathbf{\Omega}, \mathbf{D} = \mathbf{D}^e + \mathbf{D}^p, \mathbf{\Omega} = \mathbf{\Omega}^e + \mathbf{\Omega}^p \quad (3)$$

where \mathbf{D} and $\mathbf{\Omega}$ are the symmetric rate of stretching tensor and antisymmetric spin rate tensor, respectively. \mathbf{D}^e and \mathbf{D}^p are the elastic and plastic part of \mathbf{D} , while $\mathbf{\Omega}^e$ and $\mathbf{\Omega}^p$ are the elastic and plastic part of $\mathbf{\Omega}$.

\mathbf{F}^p is related to the shear strain rate on specific slip systems [34, 35]:

$$\mathbf{L}^p = \dot{\mathbf{F}}^p \cdot \mathbf{F}^{p-1} = \sum_{\alpha=1}^N \dot{\gamma}^\alpha \mathbf{s}^\alpha \mathbf{m}^\alpha \quad (4)$$

$$\mathbf{s}^{*\alpha} = \mathbf{F}^e \cdot \mathbf{s}^\alpha, \mathbf{m}^{*\alpha} = \mathbf{m}^\alpha \cdot \mathbf{F}^{e-1} \quad (5)$$

$$\mathbf{P}^\alpha = \frac{1}{2} (\mathbf{s}^{*\alpha} \mathbf{m}^{*\alpha} + \mathbf{m}^{*\alpha} \mathbf{s}^{*\alpha}), \mathbf{W}^\alpha = \frac{1}{2} (\mathbf{s}^{*\alpha} \mathbf{m}^{*\alpha} - \mathbf{m}^{*\alpha} \mathbf{s}^{*\alpha}) \quad (6)$$

$$\mathbf{D}^p = \sum_{\alpha=1}^N \mathbf{P}^\alpha \dot{\gamma}^\alpha, \mathbf{\Omega}^p = \sum_{\alpha=1}^N \mathbf{W}^\alpha \dot{\gamma}^\alpha \quad (7)$$

where $\dot{\gamma}^\alpha$, \mathbf{s}^α and \mathbf{m}^α are respectively the shear strain rate, unit slip direction vector and slip plane normal vector of the slip system α in the reference configuration. $\mathbf{s}^{*\alpha}$ and $\mathbf{m}^{*\alpha}$ are the slip direction and normal direction of the slip plane for the slip system α in the deformed lattice, respectively. N is the number of active slip systems, which is 12 for {111}<110> octahedral slip systems in this study.

The elastic constitutive law is given by [34]:

$$\overset{\nabla}{\boldsymbol{\tau}}^e = \mathbf{C} : \mathbf{D}^e \quad (8)$$

$$\overset{\nabla}{\boldsymbol{\tau}}^e = \dot{\boldsymbol{\tau}} - \boldsymbol{\Omega}^e \cdot \boldsymbol{\tau} + \boldsymbol{\tau} \cdot \boldsymbol{\Omega}^e, \overset{\nabla}{\boldsymbol{\tau}} = \dot{\boldsymbol{\tau}} - \boldsymbol{\Omega} \cdot \boldsymbol{\tau} + \boldsymbol{\tau} \cdot \boldsymbol{\Omega} \quad (9)$$

$$\overset{\nabla}{\boldsymbol{\tau}} = \mathbf{C} : \mathbf{D}^e - \sum_{\alpha=1}^N \left(\mathbf{W}^\alpha \cdot \boldsymbol{\tau} - \boldsymbol{\tau} \cdot \mathbf{W}^\alpha \right) \dot{\gamma}^\alpha \quad (10)$$

where $\overset{\nabla}{\boldsymbol{\tau}}^e$ and $\overset{\nabla}{\boldsymbol{\tau}}$ are the Jaumann rate of Kirchhoff stress according to $\boldsymbol{\Omega}^e$ and $\boldsymbol{\Omega}$ respectively, while $\dot{\boldsymbol{\tau}}$ is the material stress rate. \mathbf{C} is the tensor of elastic moduli, which consists of three dependent constants (i.e. C_{11} , C_{12} and C_{44}) for face-centred cubic materials [36].

The shear strain rate is described by a viscoplastic phenomenological power law [37] :

$$\dot{\gamma}^\alpha = \dot{\gamma}_0 \left| \frac{\tau^\alpha - \chi^\alpha}{\tau_c^\alpha} \right|^n \text{sign}(\tau^\alpha - \chi^\alpha) \quad (11)$$

where $\dot{\gamma}_0$ is the reference shear strain rate, n is the rate sensitivity exponent. τ^α , τ_c^α and χ^α are the resolved shear stress (RSS), critical resolved shear stress (CRSS) and backstress of the slip system α , respectively. The RSS on the slip system is calculated based on Schmid's law.

$$\tau^\alpha = \mathbf{m}^{*\alpha} \cdot \boldsymbol{\tau} \cdot \mathbf{s}^{*\alpha} = \mathbf{P}^\alpha : \boldsymbol{\tau} \quad (12)$$

$$\boldsymbol{\tau} = \det(\mathbf{F}) \boldsymbol{\sigma} \quad (13)$$

where $\boldsymbol{\tau}$ is the Kirchhoff stress and can be calculated by the Cauchy stress $\boldsymbol{\sigma}$.

The isotropic hardening/softening is described via the evolution of CRSS following Voce type function [38, 39]:

$$\dot{\tau}_c^\alpha = \sum_{\beta} h_{\alpha\beta} |\dot{\gamma}^\beta|, h_{\alpha\beta} = h(\gamma) [q + (1-q)\delta_{\alpha\beta}] \quad (14)$$

$$h(\gamma) = h_0 \left(1 - \frac{\tau_0}{\tau_s} \right) \exp \left(-\frac{h_0 \gamma}{\tau_s} \right), \gamma = \sum_{\alpha=1}^N \int_0^t |\dot{\gamma}^\alpha| dt \quad (15)$$

where $\delta_{\alpha\beta}$, $h_{\alpha\alpha}$ and $h_{\alpha\beta}$ are Kronecker delta, self and latent hardening modulus respectively, γ is the sum of the accumulated plastic slip on all slip systems. q is the ratio of latent hardening moduli to self hardening moduli and ranges from 1 to 1.4 usually [34]. It is set to 1 in this

study according to Ni-based alloy GH4169 in literature [40]. h_0 , τ_0 and τ_s are the initial hardening moduli, the initial and saturated value of CRSS, respectively.

The non-linear kinematic hardening is characterized by Armstrong-Frederick [41] type backstress, which is widely used in crystal plasticity constitutive model to account for Bauschinger effect.

$$\dot{\chi}^\alpha = C\dot{\gamma}^\alpha - D\chi^\alpha |\dot{\gamma}^\alpha| \quad (16)$$

where C and D are direct hardening moduli and dynamic recovery coefficient respectively.

The crystal plasticity constitutive model above has been implemented in ABAQUS/Standard by user-material subroutine (UMAT).

3.2 Constitutive parameters calibrations

Uniaxial FGH4098 alloy LCF data which was obtained from LCF tests with a strain range of 2% and a strain ratio of -1 was selected to calibrate constitutive parameters at 650°C and 750°C, and can be found in our previous study [30]. On account of huge computational time consumption of CPFE simulation, a representative volume element (RVE) consisting of 512 cubic grains with 27 C3D8 elements per grain was generated to conduct parameter calibration, which balances equivalence and efficiency [42], as shown in Fig. 4(a). The detailed verification of effectiveness for cubic RVE in obtaining stress-strain response and convergence analysis of element size is shown in Fig. A. 1 and Fig. A. 2. Grain orientations were selected from EBSD measurement data, and almost randomly distributed due to texture-free attribute of this material as shown in Fig. 4 (b). The periodical boundary constraints are assigning on the opposite faces of the RVE by Python scripts. Then the average stress-strain responses were extracted from the master point to fitting experiment data using “trial-and-error” method by minimizing the difference between experimental and simulated strain-stress curves [40]. There are ten parameters in total including three elastic constants, two rate dependent, three isotropic and two kinematic parameters to be determined. First of all, elastic constants are obtained by fitting the macro elastic modulus according to Equation.(17) [36, 43]. And E , ν and A are elastic moduli along $\langle 100 \rangle$ direction, Poisson ratio and anisotropy coefficient for crystal Ni respectively. It should be noted that elastic anisotropy plays an important role in strain localization and is correlated with A . When A equals 1, the material is isotropic. The anisotropy coefficient A is set as 2.57 here according to literature [36]. Next,

rate dependent parameters are determined by fitting the stress relaxation behaviour during the dwell period [44]. Then isotropic and kinematic hardening parameters are determined by fitting experimental hysteresis curves [45]. The comparison between experimental and simulated strain-stress curves at 650°C and 750°C is shown in Fig. 5, indicating a good agreement. The obtained parameters are listed in Table 1.

$$C_{11} = \frac{E(1-\nu)}{1-\nu-2\nu^2}, C_{12} = \frac{E\nu}{1-\nu-2\nu^2}, C_{44} = \frac{A}{2}(C_{11} - C_{12}) \quad (17)$$

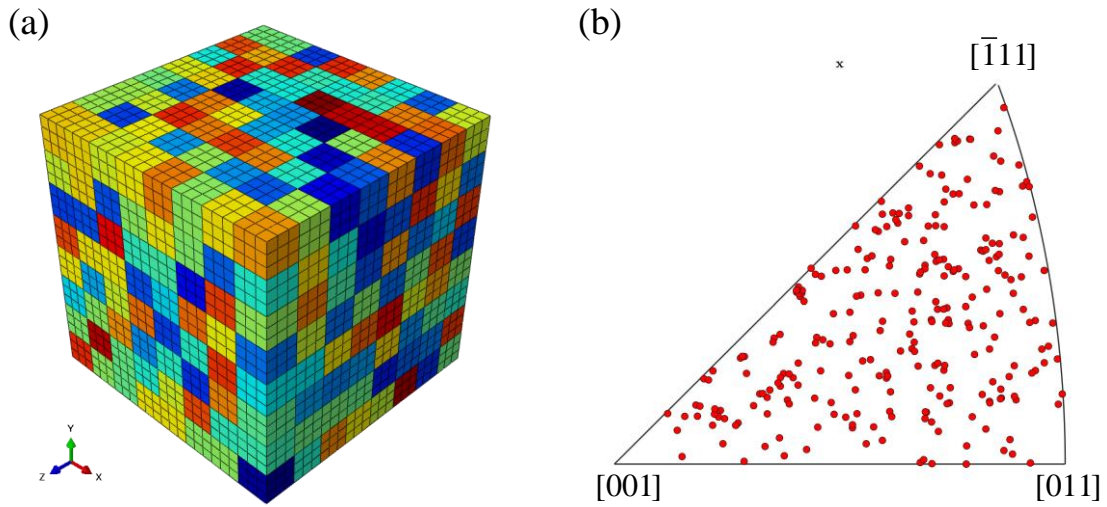


Fig. 4 (a) Cubic RVE used for parameter calibration. The colours represent different crystallographic orientations. (b) The IPF for orientation of grains in the cubic RVE along x axial.

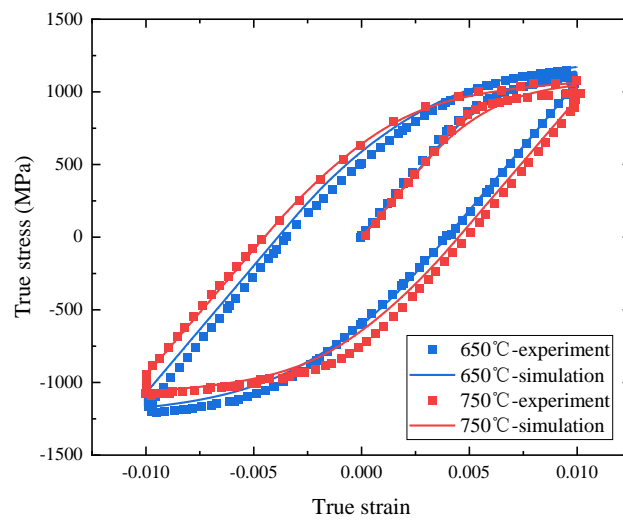


Fig. 5 Comparison between experimental and simulated strain-stress curves at 650°C and 750°C. The experimental data can be found in the previous study [30].

Table 1 Constitutive model parameters for FGH4098 at 650°C and 750°C.

Parameter	Unit	650°C	750°C
C_{11}	MPa	185621.8	183057.3
C_{12}	MPa	109016.0	107509.8
C_{44}	MPa	98438.5	97078.5
$\dot{\gamma}_0$	s^{-1}	0.001	0.001
n	-	40	30
τ_0	MPa	300	250
τ_s	MPa	310	260
h_0	MPa	600	600
C	MPa	96000	150000
D	-	600	1000

3.3 Polycrystalline aggregate models and fatigue indicator parameters

A polycrystalline aggregate orphan mesh model with an area of $400 \times 400 \mu m^2$ containing 549 grains was reconstructed via reading the EBSD file with software Dream.3D [46]. Due to lacking subsurface grain morphology and orientation data, a simplified Quasi-3D model containing 160000 C3D8 elements with one element in the direction perpendicular to the surface was established, as schematically shown in Fig. 6. The element size is $1 \mu m$, which is surmised to be small enough to capture grain boundary and local microstructure features. Since the finite element model is based on the real microstructure of FGH4098, the effects of grain size, annealing twin boundary and texture on deformation behaviour can be taken into consideration all together. Different from the RVE in Section 3.2 to consider convergence of average stress-strain response, the polycrystalline aggregate here is aimed at investigating mesoscale deformation and damage. According to the study by Prithivirajan and Sangid [5], minimum number of grains within the polycrystalline aggregate to obtain reliable estimates of mesoscale mechanical fields and corresponding fatigue lives is about 200. Therefore, it can be deduced that the polycrystalline aggregate here is large enough to reflect microstructure features and mesoscale field quantities in a statistical sense. The constitutive model parameters in Table 1 and mean crystallographic orientations obtained from EBSD measurement were assigned to each grain by Python script. The left, bottom and back surface

of the model were fixed in the x, y and z direction respectively to remove rigid body displacement, and the uniformly distributed external load was imposed on the right surface which was consistent with the LCF testing conditions. Considering intensive computational consumption, most CPFE modelling under cyclic loading in literature is limited to several cycles [5, 6, 19]. Hence, only 15 cycles were modelled here which allowed the deformation to reach the stabilized state to reveal the heterogeneity of mesoscale parameters.

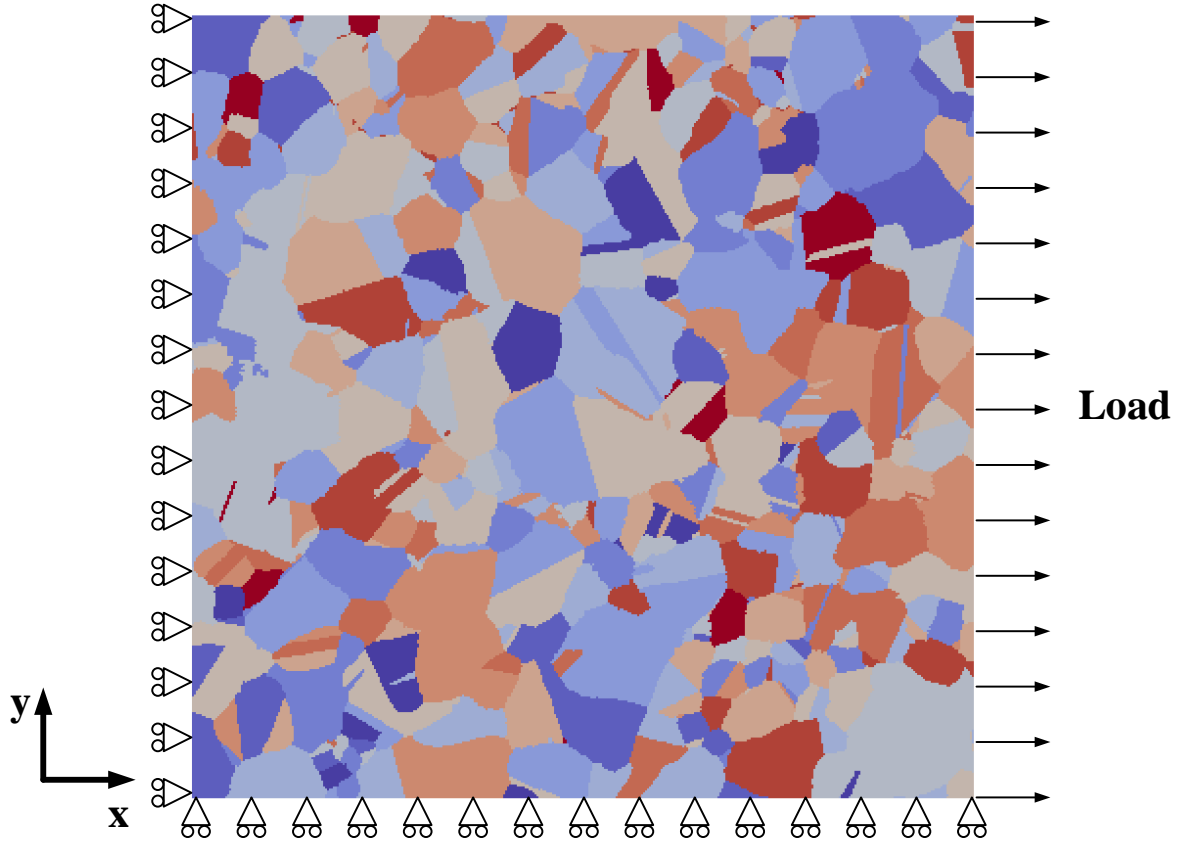


Fig. 6 Finite element model and boundary conditions of the FGH4098 alloy with an area of $400 \times 400 \mu\text{m}^2$. The colours represent different crystallographic orientations.

Under the framework of CPFE, mesoscale parameters such as shear strain, RSS, and normal stress on specific slip systems can be combined to form fatigue indicator parameters (FIPs) which represent the driving forces for fatigue crack nucleation and microstructurally small crack growth [3, 19]. Two FIPs are introduced in present study to evaluate the the possibility of fatigue failure at grain scale. The first one is the ASSEDD proposed by Korsunsky [22] and can be expressed as

$$W_p = \sum_{\alpha=1}^N \int \tau^{\alpha} \dot{\gamma}^{\alpha} dt \quad (18)$$

in which τ^α and $\dot{\gamma}^\alpha$ are the RSS and shear strain rate on the slip system α , N is the number of all active slip systems.

The second metric is developed by McDowell and his co-workers [23, 24, 47], based on the critical plane method proposed by Fatemi and Socie [48], and given by

$$P_{FS} = \frac{\Delta\gamma_{\max}^p}{2} \left(1 + k \frac{\sigma_n^{\max}}{\sigma_y} \right) \quad (19)$$

$$\sigma_n^\alpha = \mathbf{m}^\alpha \cdot \boldsymbol{\sigma} \cdot \mathbf{m}^\alpha \quad (20)$$

where $\Delta\gamma_{\max}^p$ is the maximum range of cyclic plastic shear strain on the specific slip system, σ_n^{\max} is peak stress normal to the slip plane, σ_y is the yield strength and k is a constant that controls the influence of normal stress, which is set as 0.5 [24]. Normal stress on the slip system α can be calculated by Eq.(20), in which \mathbf{m}^α is the unit normal vector of the slip plane and $\boldsymbol{\sigma}$ is the stress tensor at the integrate points of each element.

4. Results and discussion

4.1 Macro deformation and fractography analysis

Results of low cycle fatigue tests are presented in Table 2. The cyclic stress-strain behaviours of the FGH4098 alloy at 650°C and 750°C are shown in Fig. 7. The peak and valley stresses are plotted in Fig. 7 (a) as a function of the number of cycles, and experience a stabilized state after undergoing cyclic softening at the early stage of fatigue loading, until entering the final fracture regime. Hence, stress-strain hysteresis loops and stress-time curves in the mid-life cycle are selected to comparatively study the effects of temperatures on macro mechanical behaviour. The hysteresis loops of all specimens are quite thin and narrow, manifesting limited plastic deformation. The area of stress –strain hysteresis loops at 750°C are larger than that at 650°C, with lower peak stress values, owing to material softening at higher temperature. Unlike the obvious stress relaxation at a trapezoidal wave loading with a 2% strain range and strain ratio of -1 in previous study [30], there is no obvious stress relaxation found in current study maybe due to the lower load level.

The area of a hysteresis loop is the energy dissipation density (EDD) per cycle, which is widely used as a macro fatigue criterion for life prediction and can be calculated according to

Eq. (21). Generally, only the plastic strain in total strain range contributes to damage in low cycle fatigue, and just a part of total energy dissipation works in damage [49]. However, as discussed by Korsunky [22], this part depends on total EDD as well, this parameter is therefore selected to evaluate macroscale deformation and damage. Fig. 8 shows the evolution of EDD per cycle as well as the accumulated values over fatigue cycles. Due to the fluctuation of stress-strain hysteresis loops during cyclic loading, the EDD values from 250th cycles to mid-life cycles are averaged to obtain stabilized values, which are summarized in Table 2. The accumulated EDD calculated by Eq.(22), increase almost linearly in that EDD per cycle varies slightly above and below the mean value. The stabilized EDD can reasonably explain that higher temperature leads to more damage at the same strain level and shorter fatigue life, as given in Table 2.

$$w = \oint \sigma d\varepsilon \quad (21)$$

$$W = \sum_{i=1}^N w_i \quad (22)$$

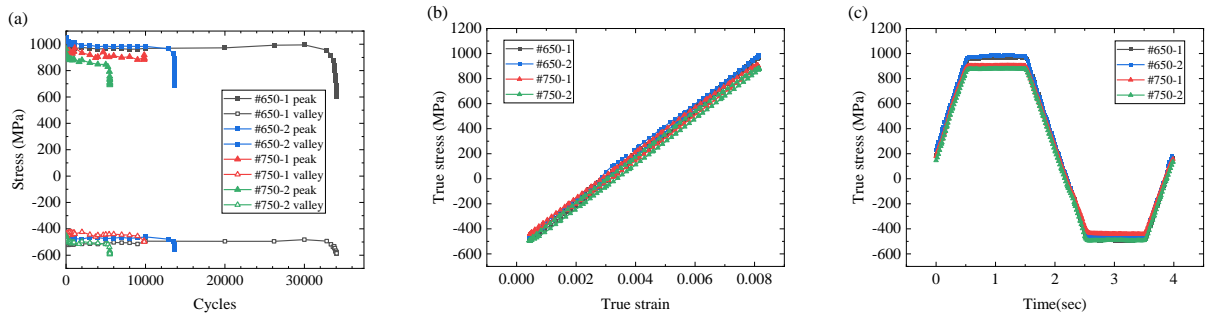


Fig. 7 (a) Peak and valley stress against number of cycles with a strain rate of 0.78%/s during the loading and unloading stage. (b) Stress-strain hysteresis curves and (c) stress-time curves in the mid-life cycle (i.e. 20000th, 7000th, 5000th, 3000th for #650-1, #650-2, #750-1, #750-2 respectively).

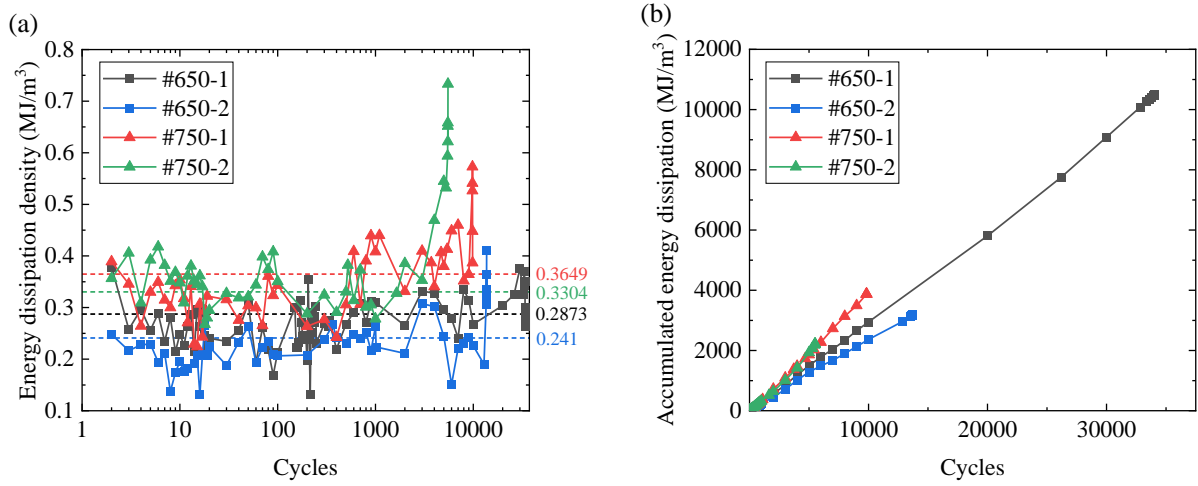


Fig. 8 (a) Strain energy dissipation density and (b) accumulated energy dissipation density against number of cycles.

Table 2 Results of LCF tests.

Number	σ_{\max} /MPa	σ_{\min} /MPa	Fatigue life /cycle	$w_{\text{stabilized}}$ / ($\text{MJ} \cdot \text{m}^{-3}$)
#650-1	974	-503	34062	0.2873
#650-2	964	-473	13703	0.2410
#750-1	926	-438	9841	0.3649
#750-2	866	-510	5519	0.3304

SEM fractographic images of all tested specimens are shown in Fig. 9. As a result of the colour differences induced by oxidation at high temperature, the fracture surfaces can be evidently divided into three regions, i.e. crack initiation site (CIS), crack propagation region (CPR) and final fracture region (FFR) indicated in Fig. 9. It can be seen from Fig. 9 that fatigue cracks mainly initiate and propagate transgranularly (although the crystallographic facets are not as evident as observed at room temperature), indicating that slip deformation is the dominant failure mechanism at the investigated loading conditions for both temperatures, which is in line with CPFGE theory above.

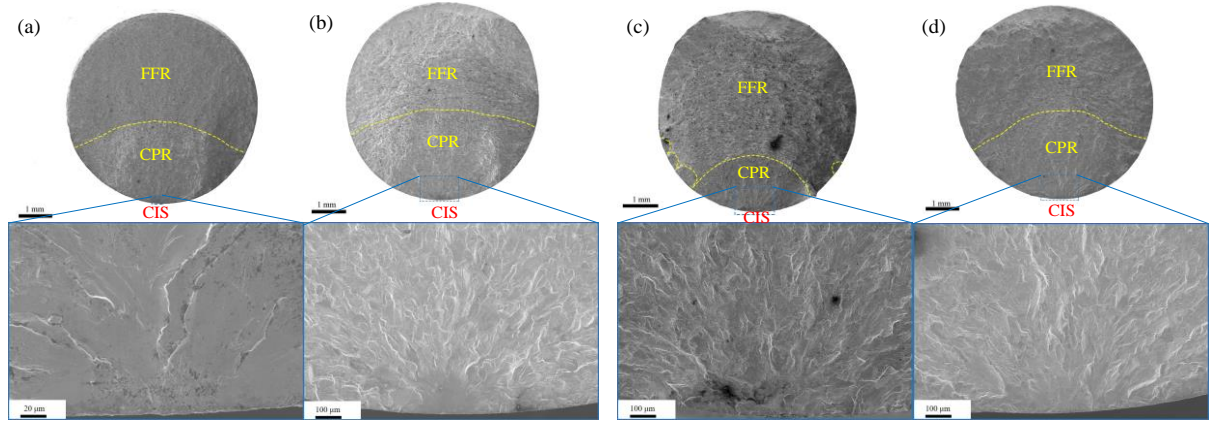


Fig. 9 SEM fractographic images of FGH4098 specimens at 650°C and 750°C: (a) #650-1, (b) #650-2, (c) #750-1, (d) #750-2.

4.2 Assessment of misorientation parameters

In order to evaluate the influence of temperatures on global and local deformation, four AOI selected from #650-2 and #750-2 specimens are used for EBSD characterization as illustrated in Fig. 2 (b). The KAM is calculated based on local misorientation of neighbour pixels in grains representing the local lattice orientation rotation, and serving as an indicator of plastic deformation [9, 31]. Fig. 10 shows the crystallographic morphology, KAM and GND density distribution of specimen #650-2. Both KAM and GND density are distributed heterogeneously, owing to the varying grain orientations and grain boundary characters in the polycrystalline structure. However, the KAM legend has a peak value of 2, which demonstrates the limited plastic deformation in both regions. As to the AOI2, a slightly higher KAM value can be found along the crack surface and free surface on the left side. Similar KAM and GND density distribution features are also found for specimen #750-2 as shown in Fig. 11. In order to quantify the influence of temperatures on deformation characteristics, histograms of KAM and GND density are drawn in Fig. 12. KAM and corresponding GND density values in AOI 2 are obviously higher than those in AOI 1 due to more severe deformation at the crack initiation site at the same temperature. Those misorientation parameters in the AOI 1 at 650°C are roughly similar to those at 750°C (slightly higher). However, for the AOI 2, the KAM and GND density values at 750°C are evidently higher, reflecting increased local deformation and damage, and thus contributing to shorter life times (compared to 650°C).

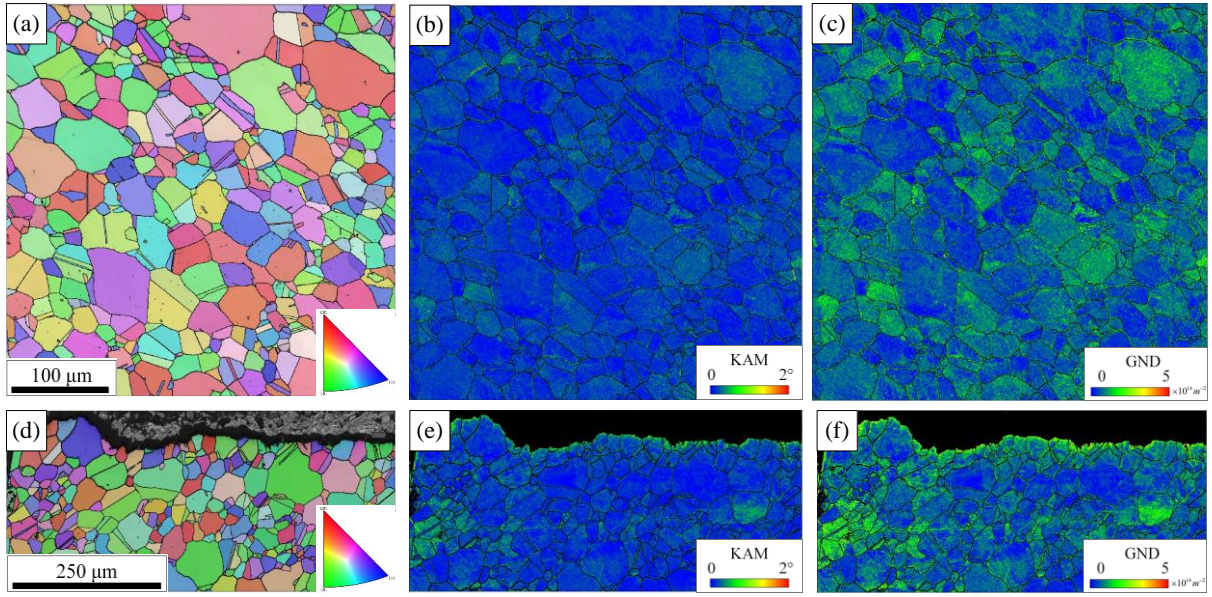


Fig. 10 IPF map, KAM map and GND density map of specimen #650-2 for (a)-(c) AOI 1 and (d)-(f) AOI 2.

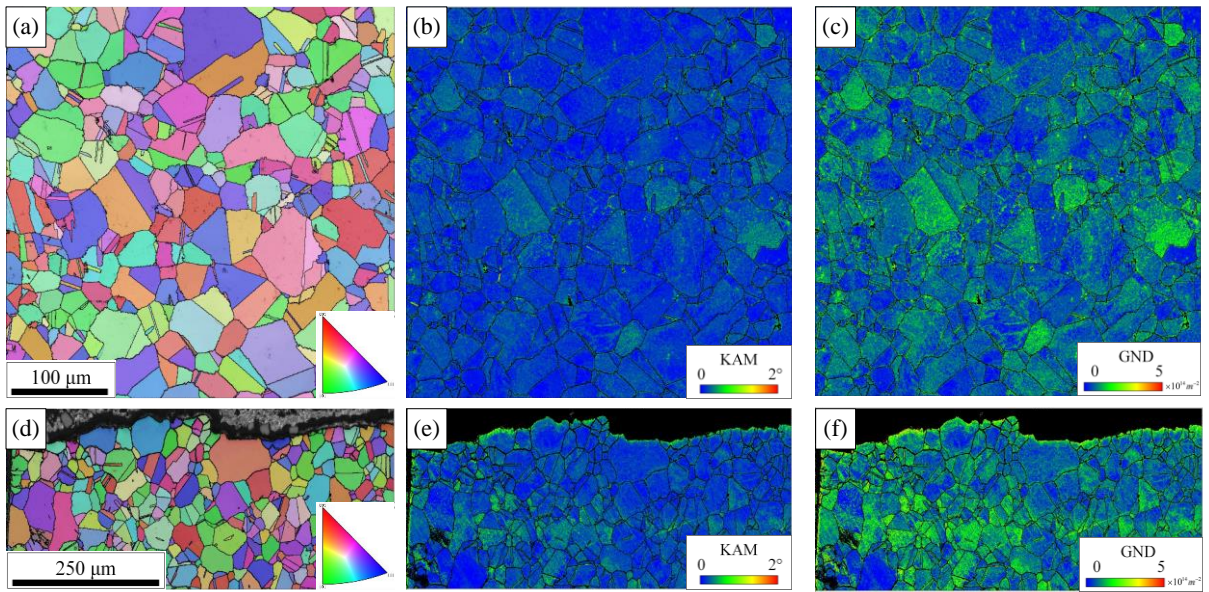


Fig. 11 IPF map, KAM map and GND density map of specimen #750-2 for (a)-(c) AOI 1 and (d)-(f) AOI 2.

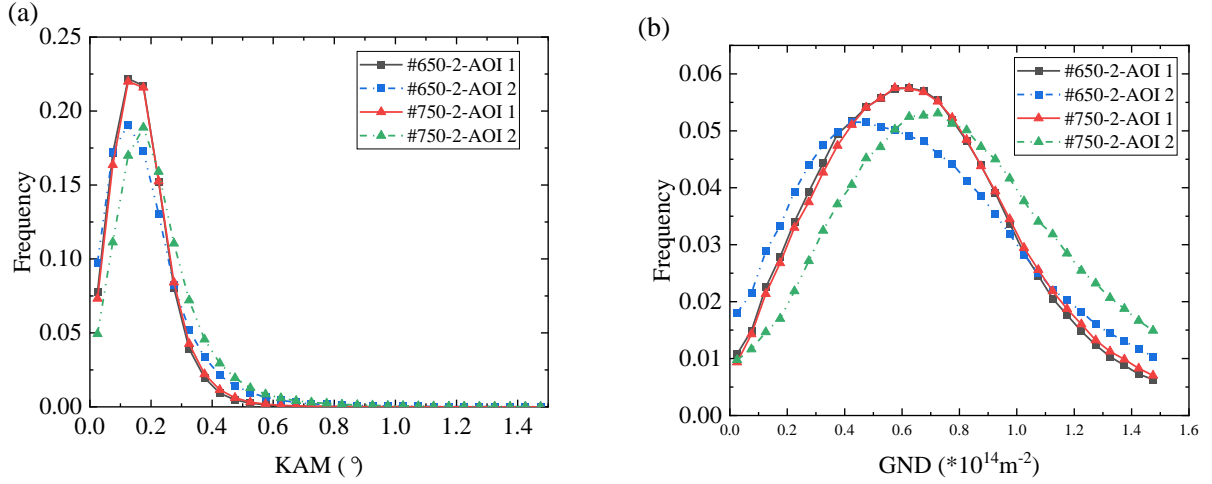


Fig. 12 Histograms of (a) KAM and (b) GND density in two regions at 650°C and 750°C.

4.3 Quantitative assessment of FIPs

In the polycrystalline aggregate, grains are anisotropic in both elasticity and plasticity due to different crystalline orientations, and then can be categorized as hard grains and soft grains [50]. Fig. 13 (a) shows the elastic modulus map along the loading direction, i.e. x-axis. Elastic moduli of each grain along any orientation $[ijk]$ can be calculated using the compliance matrix and the mean crystallographic orientation of each grain [51, 52]:

$$\frac{1}{E_{ijk}} = S_{11} - 2 \left(S_{11} - S_{12} - \frac{S_{44}}{2} \right) \left(l_{i1}^2 l_{j2}^2 + l_{j2}^2 l_{k3}^2 + l_{k3}^2 l_{i1}^2 \right) \quad (23)$$

where S_{11}, S_{12}, S_{44} are compliance constants and can be calculated from elastic constants in Table 1 by matrix inversion operation. And l_{i1}, l_{j2} and l_{k3} are the direction cosine of $[ijk]$ in the crystal system. Converting the unit vector in the load direction from the global system to the crystal system, elastic moduli along this direction of each grain can be obtained, which has been integrated into in-house codes in MTEX [31].

The blue colour represents low elastic modulus corresponding to soft grains, while the yellow colour corresponds to hard grains conversely. These hard-soft combinations lead to heterogeneous distribution of stress and strain, as shown in Fig. 13 (b) and (c). Contour plots are processed by Python scripts with a jet spectrum. Harder grains take on higher stress and lower strain level. Obvious stress concentration can be found at grain boundaries, annealing

twin boundaries and triple points resulting from deformation mismatch of these highly misoriented neighbouring grains.

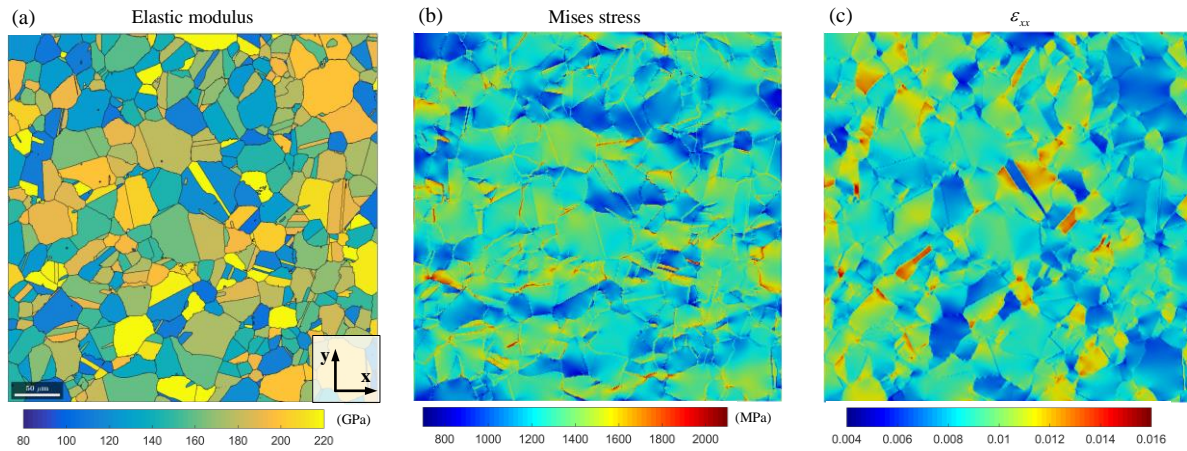


Fig. 13 (a) Elastic modulus map along the loading direction. Contour plots of (b) Mises stress and (c) strain component in the loading direction at the maximum applied load after 15 fatigue cycles at 650°C.

Two FIPs are selected to evaluate the influence of temperature on deformation and damage levels, as described in Section 3.3. They both consider the combined influence of strain and stress components rather than strain only, compared with the accumulated plastic strain. Fig. 14 (a) and (b) show the ASSEDD after 15 cyclic loadings at 650°C and 750°C, respectively, while Fig. 14 (d) and (e) show the field distribution of Fatemi-Socie parameter. These two FIPs at different temperatures are plotted with the same legend for direct comparison. Both the ASSEDD and Fatemi-Socie parameter predict severer slip deformation and damage at higher temperature, resulting in higher propensity of fatigue failure. In order to quantify the heterogeneity of deformation and damage, the FIPs are normalized by the mean values, and the corresponding histograms are plotted in Fig. 14 (c) and (f). The value of two FIPs in each integrate point, which are predefined in UMAT, are extracted from calculative results of ABAQUS/Standard. Then the mean value and normalized FIPs are calculated for both 650°C and 750°C. The histograms show the distribution of normalized FIPs at 750°C are more homogeneous than that at 650°C, suggesting a larger population of grains control the fatigue life. The hot spots predicted by the two FIPs are consistent in general and mainly observed in the vicinity of grain boundaries and annealing twin boundaries.

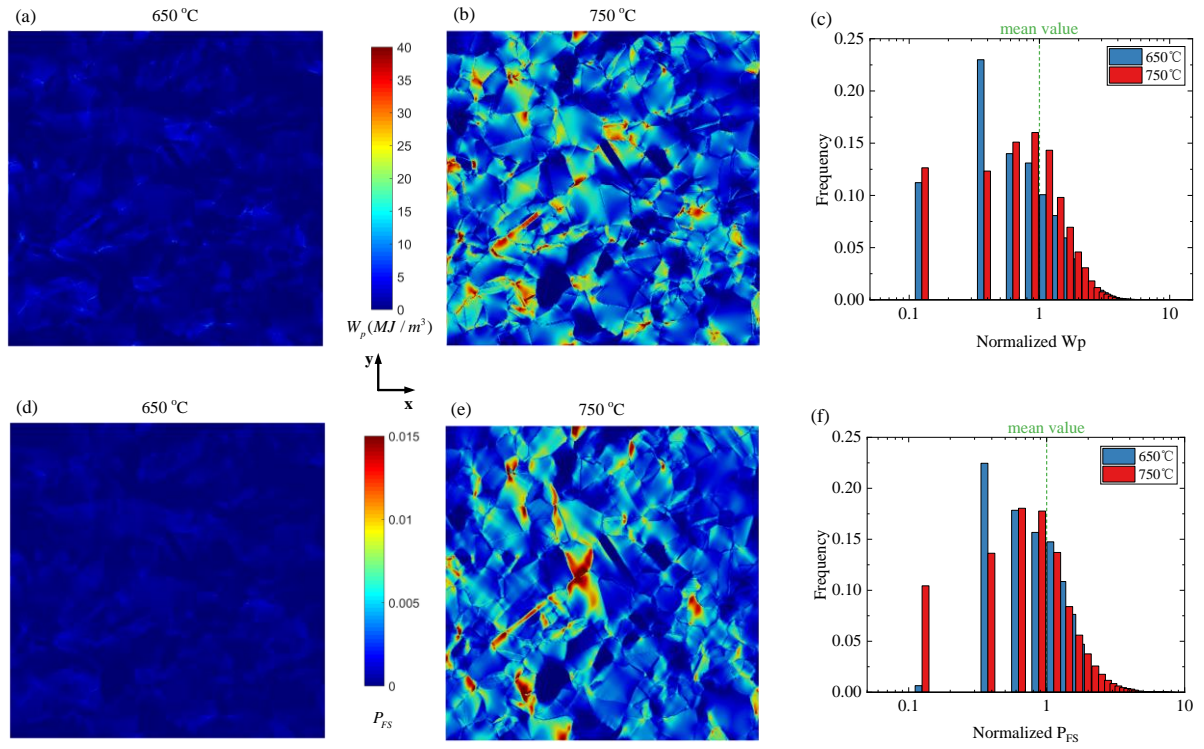


Fig. 14 Contour plots of ASSEDD (a) at 650°C, (b) at 750°C, Fatemi-Socie parameter (d) at 650°C, (e) at 750°C after 15 cyclic loadings. Histograms of (c) the normalized ASSEDD and (f) Fatemi-Socie parameter in the stabilized cycle.

It should be noted that, the Fatemi-Socie parameter is calculated in the stabilized cycle, while the ASSEDD is obtained by integration throughout the cyclic loadings. Hence, the ASSEDD can be used for assessment of deformation and damage evolution during cyclic loadings. Four hot spots in different positions undergoing diverse stress states are selected, as shown in Fig. 15 (a). The ASSEDD is plotted as a function of the number of cycles at 650°C and 750°C in Fig. 15 (b) and (c), respectively. It can be seen that the ASSEDD increase nearly linearly with the number of cycles. The ASSEDD growth rates at hot spots with different positions are disparate, and much higher numerically at 750°C than that at 650°C. Furthermore, even though in the same position, the growth rates are somewhat different owing to the various distribution and evolution of stress-strain states at mesoscale resulting from different constitutive parameters at the two investigated temperatures.

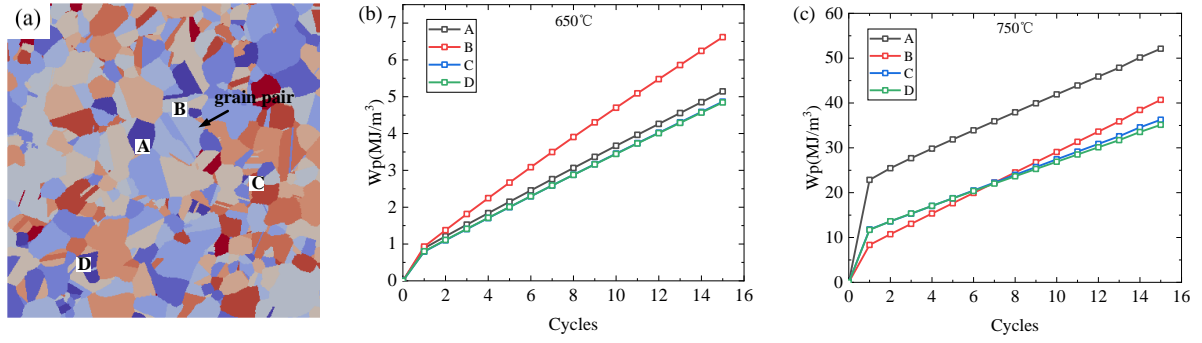


Fig. 15 (a) Schematic locations of selected hot spots. ASSEDD versus cycles for four hot spots at (b) 650°C and (c) 750°C.

4.4 Effect of annealing twin boundaries

Annealing twin boundaries are prominent features in PM Ni-based superalloys formed during heat treatment processing due to the low stacking fault energy of Ni-based superalloys and play an important role in crack initiation [53, 54]. Generally, in the scenario of natural fatigue crack initiation without inclusions or artificial micro-notches, cracks are prone to initiate in large favourably oriented grains in the vicinity of annealing twin boundaries [55-57]. Moreover, $\Sigma 3$ twin boundary is parallel to $\{111\}$ slip plane and elastic anisotropy induced by twin and parent grain pairs contribute to the stress-strain concentration and potentially fatigue failure [6, 7, 58]. There is a threshold value for the difference in elastic modulus, below which no crack initiation will occur [7]. Hence, a typical twin and parent grain pair with high difference of elastic modulus in the polycrystalline aggregate is selected for detailed analysis, as shown in Fig. 15 (a) and Fig. 16 (a). The twin and parent grain orientations are plotted on IPF maps of elastic modulus and Schmid factor contours, as shown in Fig. 16(b) and (c). Fig. 17 shows strain component ε_{xx} , ASSEDD and Fatemi-Socie parameter at 650°C after 15 cyclic loadings along the path P-P' depicted in Fig. 16(a). It can be seen that, the peak value of normal strain component occurs slightly offset the twin boundaries on the elastically soft side. Similar distribution of ASSEDD and Fatemi-Socie parameter can be found along the path, i.e. high damage values take place in the vicinity of twin boundaries, which is consistent with the SEM-DIC experiment results in literature [7, 57, 59].

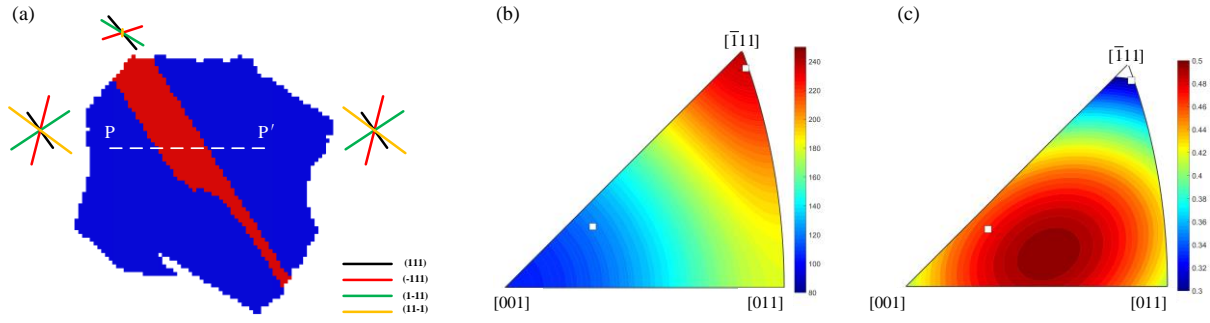


Fig. 16 (a) A typical large grain containing annealing twin boundary. The corresponding $\{111\}$ slip traces of the twin and parent grain pair are plotted with different colours, with the length of lines representing relative magnitude of Schmid factors. Iso-curves of (b) the elastic modulus (c) Schmid factors of the $\{111\}\langle 110 \rangle$ slip systems along the loading direction.

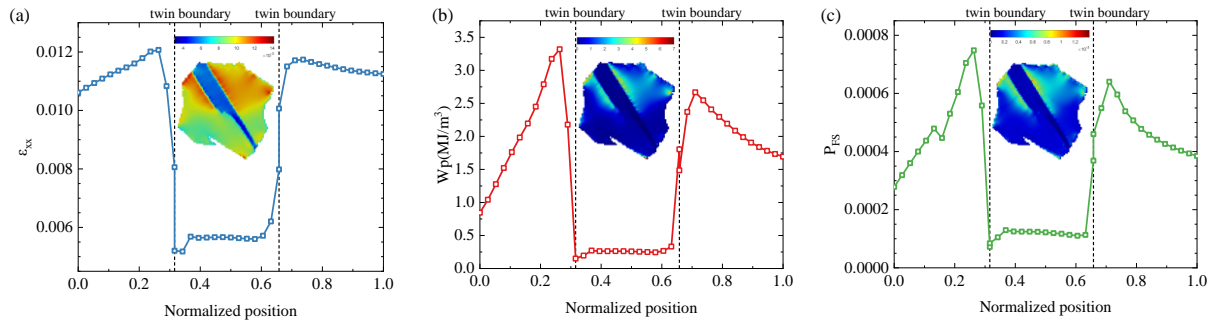


Fig. 17 (a) Strain component ϵ_{xx} (b) ASSEDD and (c) Fatemi-Socie parameter along the path P-P' depicted in Fig. 16 (a) at 650°C after 15 cyclic loadings. Vertical dotted lines represent the position of twin boundaries.

5. Summary and conclusions

In this study, the low cycle fatigue behaviour of a PM Ni-based superalloy FGH4098 was investigated by EBSD analysis and CPFE simulation at 650°C and 750°C. Key findings of this research are summarized as follows:

(1) In regard to macro deformation under LCF, specimens at 750°C possess higher plastic deformation, i.e. higher EDD value, resulting in shorter fatigue life than that at 650°C under the same strain load level.

(2) The KAM and derived GND density distribution of specimens tested at 650°C and 750°C are similar in the centre of the transverse plane. However, in the crack initiation regions the specimen tested at 750°C exhibits higher KAM and GND density values.

(3) Two FIPs, ASSEDD and Fatemi-Socie parameter, are introduced into CPFE frameworks and confirmed higher and more homogeneous LCF deformation and damage at 750°C compared to those at 650°C. The evolution rates of ASSEDD at hot spots with various stress states are different, and higher rates are found at higher temperatures.

(4) More intense deformation and damage are found in the soft side of the twin and parent grain pair, and slightly offsets the annealing twin boundaries.

Dataset Statement

The data that support the findings of this study are available from the corresponding author upon reasonable request.

Acknowledgement

The authors would like to thank the National Science and Technology Major Project (2017-VI-0008-0078; 2017-IV-0004-0041), National Natural Science Foundation of China (No. 51805251; 11872204), and the Natural Science Foundation of Jiangsu Province (No. BK20180434) for financial support. Thanks are also due to Prof. Y. W. Zhang and Prof. J. T. Liu at Central Iron and Steel Research Institute for supply of FGH4098 alloy and useful discussions.

Appendix

To verify the effectiveness of the cubic RVE in macro stress-strain response, a RVE with explicit microstructure, i.e. varying grain size, was established using Dream.3D software [46], as shown in Fig. A. 1. The grain size obeyed log- normal distribution whose mean value and standard deviation are given by $\mu = -3.278$ and $\sigma = 0.63$ according to the EBSD characterization result in Fig. 1 (d). The corresponding grain orientation data are also obtained from EBSD results to ensure texture free attribute, as shown in Fig. 4 (b). The RVE in Dream.3D has a dimension of 360 $\mu\text{m} \times 360 \mu\text{m} \times 360 \mu\text{m}$, which contains 393 grains and 46656 C3D8 elements and proved to be large enough to obtain an effective response [28].

The cubic RVEs containing 512 grains are meshed with different numbers, as shown in Fig. A. 1. The stress-strain response under a uniaxial tensile load for different models is plotted in Fig. A. 2. It can be seen that with the refinement of mesh, the response converges

gradually. There is little difference between RVE meshed with $3 \times 3 \times 3$ elements and $4 \times 4 \times 4$ elements. What's more, the cubic RVE meshed with $3 \times 3 \times 3$ elements shows good agreement with the RVE in Dream.3D.

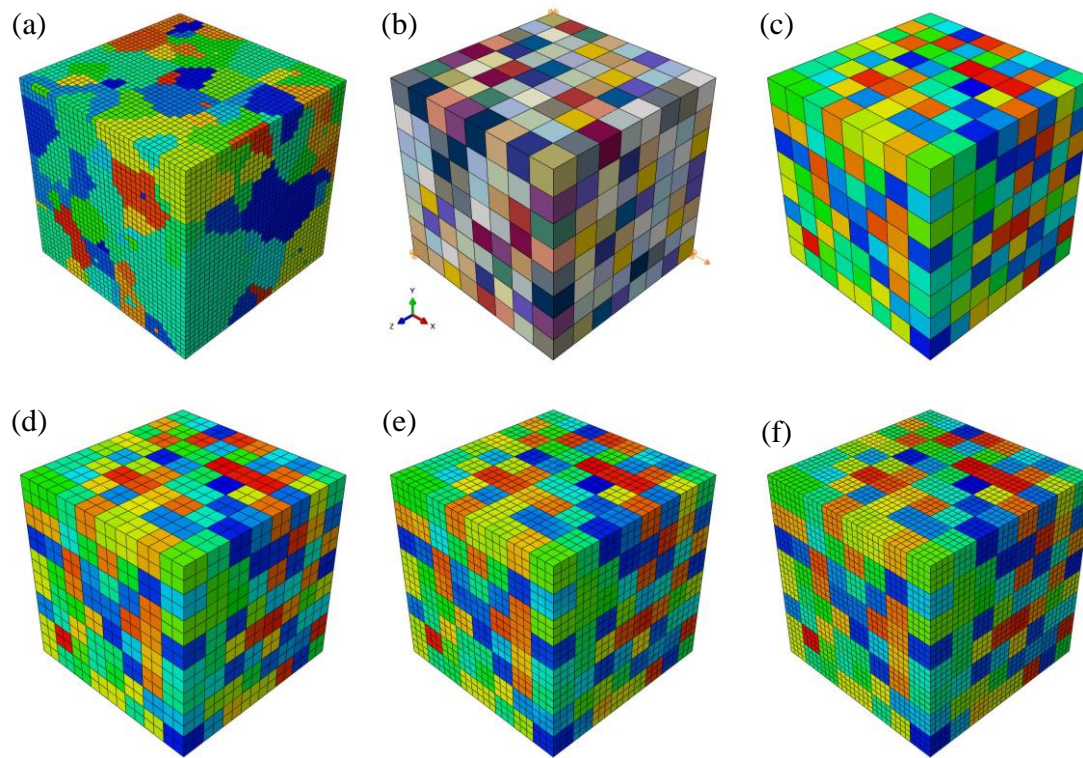


Fig. A. 1 (a) RVE modelled in Dream.3D with explicit grain structure. (b) Geometrical model of cubic RVE and meshed models with (c) $1 \times 1 \times 1$ element, (d) $2 \times 2 \times 2$ elements, (e) $3 \times 3 \times 3$ elements and (f) $4 \times 4 \times 4$ elements per grain.

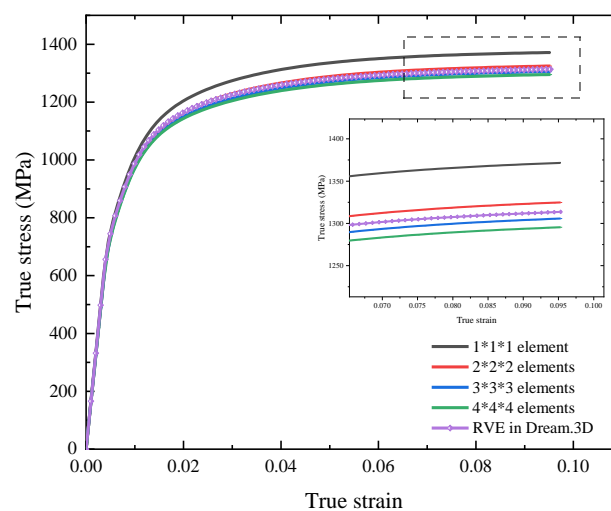


Fig. A. 2 the stress-strain response of RVE with different models under a uniaxial tensile load.

Reference

- [1] R.C. Reed, The superalloys: fundamentals and applications, Cambridge university press 2006.
- [2] R. Jiang, Y.D. Song, P.A. Reed, Fatigue crack growth mechanisms in powder metallurgy Ni-based superalloys—A review, *International Journal of Fatigue* 141 (2020).
- [3] D.L. McDowell, F.P.E. Dunne, Microstructure-sensitive computational modeling of fatigue crack formation, *International Journal of Fatigue* 32(9) (2010) 1521-1542.
- [4] R. Bandyopadhyay, M.D. Sangid, A Probabilistic Fatigue Framework to Enable Location-Specific Lifting for Critical Thermo-mechanical Engineering Applications, *Integrating Materials and Manufacturing Innovation* 10(1) (2021) 20-43.
- [5] V. Prithivirajan, M.D. Sangid, Examining metrics for fatigue life predictions of additively manufactured IN718 via crystal plasticity modeling including the role of simulation volume and microstructural constraints, *Materials Science and Engineering: A* 783 (2020).
- [6] S.R. Yeratapally, M.G. Glavicic, M. Hardy, M.D. Sangid, Microstructure based fatigue life prediction framework for polycrystalline nickel-base superalloys with emphasis on the role played by twin boundaries in crack initiation, *Acta Materialia* 107 (2016) 152-167.
- [7] J.C. Stinville, W.C. Lenthe, J. Miao, T.M. Pollock, A combined grain scale elastic-plastic criterion for identification of fatigue crack initiation sites in a twin containing polycrystalline nickel-base superalloy, *Acta Materialia* 103 (2016) 461-473.
- [8] M.A. Linne, T.R. Bieler, S. Daly, The effect of microstructure on the relationship between grain boundary sliding and slip transmission in high purity aluminum, *International Journal of Plasticity* 135 (2020).
- [9] F. Briffod, A. Bleuset, T. Shiraiwa, M. Enoki, Effect of crystallographic orientation and geometrical compatibility on fatigue crack initiation and propagation in rolled Ti-6Al-4V alloy, *Acta Materialia* 177 (2019) 56-67.
- [10] Q. Han, X. Lei, H. Yang, X. Yang, Z. Su, S.-S. Rui, N. Wang, X. Ma, H. Cui, H. Shi, Effects of temperature and load on fretting fatigue induced geometrically necessary dislocation distribution in titanium alloy, *Materials Science and Engineering: A* 800 (2021).
- [11] X. Hu, W. Ye, L. Zhang, R. Jiang, Y. Song, Investigation on creep properties and microstructure evolution of GH4169 alloy at different temperatures and stresses, *Materials Science and Engineering: A* 800 (2021).
- [12] S.-S. Rui, Y.-B. Shang, Y.-N. Fan, Q.-N. Han, L.-S. Niu, H.-J. Shi, K. Hashimoto, N. Komai, EBSD analysis of creep deformation induced grain lattice distortion: A new method for creep damage evaluation of austenitic stainless steels, *Materials Science and Engineering: A* 733 (2018) 329-337.
- [13] R.-Z. Wang, L.-Y. Cheng, S.-P. Zhu, P.-C. Zhao, H. Miura, X.-C. Zhang, S.-T. Tu, Semi-quantitative creep-fatigue damage analysis based on diffraction-based misorientation mapping and the correlation to macroscopic damage evolutions, *International Journal of Fatigue* (2021).
- [14] A. Harte, M. Atkinson, M. Preuss, J. Quinta da Fonseca, A statistical study of the relationship between plastic strain and lattice misorientation on the surface of a deformed Ni-based superalloy, *Acta Materialia* 195 (2020) 555-570.
- [15] A.J. Wilkinson, G. Meaden, D.J. Dingley, High-resolution elastic strain measurement from electron backscatter diffraction patterns: new levels of sensitivity, *Ultramicroscopy* 106(4-5) (2006) 307-13.
- [16] T. Zhang, D.M. Collins, F.P.E. Dunne, B.A. Shollock, Crystal plasticity and high-resolution electron backscatter diffraction analysis of full-field polycrystal Ni superalloy strains and rotations under thermal loading, *Acta Materialia* 80 (2014) 25-38.
- [17] Z. Zhang, D. Lunt, H. Abdolvand, A.J. Wilkinson, M. Preuss, F.P.E. Dunne, Quantitative investigation of micro slip and localization in polycrystalline materials under uniaxial tension, *International Journal of Plasticity* 108 (2018) 88-106.
- [18] R. Bandyopadhyay, A.W. Mello, K. Kapoor, M.P. Reinhold, T.F. Broderick, M.D. Sangid, On the crack initiation and heterogeneous deformation of Ti-6Al-4V during high cycle fatigue at high R ratios, *Journal of the Mechanics and Physics of Solids* 129 (2019) 61-82.

-
- [19] B. Chen, J. Jiang, F.P.E. Dunne, Is stored energy density the primary meso-scale mechanistic driver for fatigue crack nucleation?, *International Journal of Plasticity* 101 (2018) 213-229.
- [20] F.P.E.D. A. Manonukul, High- and Low-Cycle Fatigue Crack Initiation Using Polycrystal Plasticity, *Proceedings Mathematical Physical & Engineering Sciences* 460(2047) (2004) 1881-1903.
- [21] R. Bandyopadhyay, M.D. Sangid, Crystal plasticity assessment of inclusion- and matrix-driven competing failure modes in a nickel-base superalloy, *Acta Materialia* 177 (2019) 20-34.
- [22] A. Korsunsky, D. Dini, F. Dunne, M. Walsh, Comparative assessment of dissipated energy and other fatigue criteria☆, *International Journal of Fatigue* 29(9-11) (2007) 1990-1995.
- [23] M. Shenoy, J. Zhang, D.L. McDowell, Estimating fatigue sensitivity to polycrystalline Ni-base superalloy microstructures using a computational approach, *Fatigue & Fracture of Engineering Materials and Structures* 30(10) (2007) 889-904.
- [24] G.M. Castelluccio, D.L. McDowell, Microstructure-sensitive small fatigue crack growth assessment: Effect of strain ratio, multiaxial strain state, and geometric discontinuities, *International Journal of Fatigue* 82 (2016) 521-529.
- [25] V.V.C. Wan, D.W. MacLachlan, F.P.E. Dunne, A stored energy criterion for fatigue crack nucleation in polycrystals, *International Journal of Fatigue* 68 (2014) 90-102.
- [26] A. Cruzado, S. Lucarini, J. Llorca, J. Segurado, Crystal plasticity simulation of the effect grain size on the fatigue behavior of polycrystalline Inconel 718, *International Journal of Fatigue* (2018) 236-245.
- [27] M.I. Latypov, J.-C. Stinville, J.R. Mayeur, J.M. Hestroffer, T.M. Pollock, I.J. Beyerlein, Insight into microstructure-sensitive elastic strain concentrations from integrated computational modeling and digital image correlation, *Scripta Materialia* 192 (2021) 78-82.
- [28] A. Cruzado, S. Lucarini, J. Llorca, J. Segurado, Microstructure-based fatigue life model of metallic alloys with bilinear Coffin-Manson behavior, *International Journal of Fatigue* 107 (2018) 40-48.
- [29] X. Lu, F.P.E. Dunne, Y. Xu, A crystal plasticity investigation of slip system interaction, GND density and stored energy in non-proportional fatigue in Nickel-based superalloy, *International Journal of Fatigue* 139 (2020).
- [30] R. Jiang, L.C. Zhang, W.T. Zhang, Y. Zhang, Y. Chen, J.T. Liu, Y.W. Zhang, Y.D. Song, Low cycle fatigue and stress relaxation behaviours of powder metallurgy Ni-based superalloy FGH4098, *Materials Science and Engineering: A* 817 (2021).
- [31] F. Bachmann, R. Hielscher, H. Schaeben, Texture Analysis with MTEX – Free and Open Source Software Toolbox, *Solid State Phenomena* 160 (2010) 63-68.
- [32] Y. Huang, A User-Material Subroutine Incorporating Single Crystal Plasticity in the ABAQUS Finite Element Program, (1991).
- [33] J.R. Rice, Inelastic constitutive relations for solids: an internal-variable theory and its application to metal plasticity, *Journal of the Mechanics and Physics of Solids* 19(6) (1971) 433-455.
- [34] D. Peirce, R. Asaro, A. Needleman, An analysis of nonuniform and localized deformation in ductile single crystals, *Acta metallurgica* 30(6) (1982) 1087-1119.
- [35] D. Peirce, R.J. Asaro, A. Needleman, Material rate dependence and localized deformation in crystalline solids, *Acta metallurgica* 31(12) (1983) 1951-1976.
- [36] A.F. Bower, *Applied mechanics of solids*, CRC press 2009.
- [37] J.W. Hutchinson, Bounds and self-consistent estimates for creep of polycrystalline materials, *Proceedings of the Royal Society of London. A. Mathematical and Physical Sciences* 348(1652) (1976) 101-127.
- [38] S. Graff, W. Brocks, D. Steglich, Yielding of magnesium: From single crystal to polycrystalline aggregates, *International Journal of Plasticity* 23(12) (2007) 1957-1978.
- [39] L. Yin, O. Umezawa, Heterogeneous Deformation in a Commercially Pure Titanium Sheet under Dwell Fatigue Loading: Crystal Plasticity Modeling and Experiment, *ISIJ International* advpub (2021).
- [40] K.-S. Li, R.-Z. Wang, G.-J. Yuan, S.-P. Zhu, X.-C. Zhang, S.-T. Tu, H. Miura, A crystal plasticity-based approach for creep-fatigue life prediction and damage evaluation in a nickel-based superalloy, *International Journal of Fatigue* 143 (2021).

-
- [41] C.O. Frederick, P.J. Armstrong, A mathematical representation of the multiaxial Bauschinger effect, *Materials at High Temperatures* 24(1) (2007) 1-26.
- [42] Y. Xiong, P. Karamched, C.-T. Nguyen, D.M. Collins, C.M. Magazzeni, E. Tarleton, A.J. Wilkinson, Cold creep of titanium: Analysis of stress relaxation using synchrotron diffraction and crystal plasticity simulations, *Acta Materialia* 199 (2020) 561-577.
- [43] G.M. Castelluccio, D.L. McDowell, Microstructure and mesh sensitivities of mesoscale surrogate driving force measures for transgranular fatigue cracks in polycrystals, *Materials Science and Engineering: A* 639 (2015) 626-639.
- [44] B. Lin, L.G. Zhao, J. Tong, H.J. Christ, Crystal plasticity modeling of cyclic deformation for a polycrystalline nickel-based superalloy at high temperature, *Materials Science and Engineering: A* 527(15) (2010) 3581-3587.
- [45] F. Briffod, T. Shiraiwa, M. Enoki, Nucleation and propagation modeling of short fatigue crack in rolled bi-modal Ti-6Al-4V alloy, *Materials Science and Engineering: A* 790 (2020).
- [46] M.A. Groeber, M.A. Jackson, DREAM.3D: A Digital Representation Environment for the Analysis of Microstructure in 3D, *Integrating Materials and Manufacturing Innovation* 3(1) (2014) 56-72.
- [47] G.M. Castelluccio, D.L. McDowell, Mesoscale modeling of microstructurally small fatigue cracks in metallic polycrystals, *Materials Science and Engineering: A* 598 (2014) 34-55.
- [48] A. Fatemi, D.F. Socie, A CRITICAL PLANE APPROACH TO MULTIAXIAL FATIGUE DAMAGE INCLUDING OUT - OF - PHASE LOADING, *Fatigue & Fracture of Engineering Materials & Structures* 11(3) (1988) 149-165.
- [49] R.P. Skelton, M.S.J.M.a.H.T. Loveday, A re-interpretation of the BCR/VAMAS low cycle fatigue intercomparison programme using an energy criterion, 14(1) (1997) 53-68.
- [50] K. Cheong, M. Smillie, D. Knowles, Predicting fatigue crack initiation through image-based micromechanical modeling, *Acta Materialia* 55(5) (2007) 1757-1768.
- [51] M.A. Meyers, K.K. Chawla, *Mechanical behavior of materials*, Cambridge university press 2008.
- [52] O. Engler, V. Randle, *Introduction to texture analysis: macrotexture, microtexture, and orientation mapping*, CRC press 2009.
- [53] N. Bozzolo, N. Souza, R.E. Logé, Evolution of microstructure and twin density during thermomechanical processing in a γ - γ' nickel-based superalloy, *Acta Materialia* 60(13-14) (2012) 5056-5066.
- [54] R. Jiang, N. Karpasitis, N. Gao, P.A.S. Reed, Effects of microstructures on fatigue crack initiation and short crack propagation at room temperature in an advanced disc superalloy, *Materials Science and Engineering: A* 641 (2015) 148-159.
- [55] J. Miao, T.M. Pollock, J. Wayne Jones, Microstructural extremes and the transition from fatigue crack initiation to small crack growth in a polycrystalline nickel-base superalloy, *Acta Materialia* 60(6-7) (2012) 2840-2854.
- [56] J. Miao, T.M. Pollock, J. Wayne Jones, Crystallographic fatigue crack initiation in nickel-based superalloy René88DT at elevated temperature, *Acta Materialia* 57(20) (2009) 5964-5974.
- [57] R. Jiang, F. Pierron, S. Octaviani, P.A.S. Reed, Characterisation of strain localisation processes during fatigue crack initiation and early crack propagation by SEM-DIC in an advanced disc alloy, *Materials Science and Engineering: A* 699 (2017) 128-144.
- [58] A. Heinz, P. Neumann, Crack initiation during high cycle fatigue of an austenitic steel, *Acta Metallurgica et Materialia* 38(10) (1990) 1933-1940.
- [59] J.C. Stinville, N. Vanderesse, F. Bridier, P. Bocher, T.M. Pollock, High resolution mapping of strain localization near twin boundaries in a nickel-based superalloy, *Acta Materialia* 98 (2015) 29-42.